R. Bravo; Ortiz Rossini, P.; Pérez Aparicio, JL. (2014). Incipient sediment transport for non-cohesive landforms by the discrete element method (DEM). Applied Mathematical Modelling. 38(4):1326-1337. doi:10.1016 - j.apm.2013.08.010.

Incipient Sediment Transport for Non-Cohesive Landforms by the Discrete Element Method (DEM)

R. Bravo[a,*], P. Ortiz[a], J.L. Pérez-Aparicio[b]

[a] *University of Granada, Esc. Ing. Caminos. Campus Fuentenueva. 18071 Granada, Spain*
[b] *Dep. of Continuum Mechanics and theory of Structures, Universitat Politècnica de València 46022 Valencia, Spain*

Abstract

We introduce a numerical method for incipient sediment transport past bedforms. The approach is based on the discrete element method (DEM) (Pérez-Aparicio and Bravo (2006)), simulating the micro-mechanics of the landform as an aggregate of rigid spheres interacting by contact and friction. A continuous finite element approximation (Ortiz et al. (2006)) predicts the boundary shear stress field due to the fluid flow, resulting in drag and lift forces acting over the particles. Numerical experiments verify the method by reproducing results by Shields (1936) and other authors for the initiation of motion of a single grain. A series of experiments for sediments with varying compacity and constituting piles yields enhanced relationships between threshold shear stress and friction Reynolds number, to define incipient sediment transport criterion for flows over small–scale bed morphologies.

Keywords: incipient sediment transport, discrete element method, contact problems

1. Introduction

The determination of the critical shear stress at which a sediment grain starts to move has been treated with theoretical and experimental procedures by many authors (see e.g. Shields (1936), Yalin and Karahan (1979), Wiberg and Smith (1985), Dey (1999)). The seminal contribution of Shields (1936) addresses a relationship for a non-dimensional critical shear stress in terms of the friction Reynolds number, considering a sediment grain resting on an horizontal bed. Results show a scattering mainly due to an ambiguous definition of the threshold condition, dependent on the detected number of particles in motion. Otherwise, by considering the starting movement of a single particle, an analytical formulation of the problem can be developed (see for instance, Wiberg and Smith (1985)). Notwithstanding the resulting simplified configuration, a practical formulation must still adopt some relevant assumptions. First, a realistic representation of the geometrical arrangement of non-cohesive particles needs to consider the compacity

*Corresponding author
Email addresses: rbravo@ugr.es (R. Bravo), portiz@ugr.es (P. Ortiz), jopeap@upvnet.upv.es (J.L. Pérez-Aparicio)

of the grains. Second, computation of balance of forces requires a detailed distribution of stresses transmitted by the fluid flow. As a starting point for the derivation of the approximation presented in this paper, we include in this Introduction a straightforward but comprehensive formulation of the dynamic conditions for the initiation of motion for one particle (see Subsection 1.1). The formulation describes flow action via drag and lift forces along the lines of Ling (1995), generalizing it for a given local slope with initiation of motion by rolling or lifting.

Attempts to extend the Shields diagram were focused on a variety of conditions, such as fine granular (silica and mica) solids by Mantz (1977), transition values of particle Reynolds number by Yalin and Karahan (1979), or an increased range of particle Reynolds number by Miller et al. (1977). When the grains are arranged in complex shape landforms, prediction of threshold conditions is often limited to simplified geometries (e.g. Ikeda (1982)) or to local continuous approaches (e.g. Appendix A in Ortiz and Smolarkiewicz (2006)). To make the single–particle critical condition applicable to a large number of grains constituting landforms, we introduce in Section 2 a method that simulates the micromechanics of the grains based on the Discrete Element Method (see e.g. Shi and Goodman (1985) and Pérez-Aparicio and Bravo (2006)). The DEM is particularly attractive for problems with internal discontinuous geometry, and its applicability goes from large scale rigid body problems (for example, mechanical response of rock assemblies, Shi (1988), Moosavi and Grayeli (2006)), to small scale problems (for example, granular discharge from bucket elevators, Pérez-Aparicio and Bravo (2006)). The method considers the global behavior of the particles through the single contribution of each member and the interaction of particles by friction and contact, resulting in a simple momentum balance formulation and in a simple incorporation of contact restrictions.

The aforementioned simplistic theoretical–single member–threshold criterion is essential to formulate the mechanical model for the system of particles, but has a limited use. In practice, instead, incipient transport concept is frequently assumed (Dey (1999), Wallbridge et al. (1999) and Marsh et al. (2004)). The incipient transport is defined by the stress needed for the simultaneous motion of a prescribed number of particles by reptation and saltation, before a substantial change in bed configuration is produced. The present DEM methodology incorporates an incipient transport criterion depending parametrically on established sediment fluxes mimicking the experimental counting of moving grains, and computing an average stress for the set of particles in motion. Instead of adopting a prescribed value of sediment flux as minimum flux, we generalize the procedure by computing critical stresses and corresponding shear Reynolds numbers for given percentage of particles in motion.

Intricate morphologies concern flows with geometric time-dependent boundary forcings (see e.g. Ortiz and Smolarkiewicz (2009)). However, the study of inception of movement does not require a strong coupling between flow field and evolutionary landform due to small variations of its shape, even for threshold criteria defined in terms of sediment transport rates. In this work, we compute the flow field by a continuous finite element procedure (Ortiz et al. (2006)) on an unstructured grid that takes into account complicate boundaries, but flow is updated for each Reynolds number without modifying the initial geometry.

Section 3 comprises numerical experiments. The first series of tests verifies the theoretical developments for the problem of Shields in the laminar and turbulent regimes. The Shields diagram is extended to include the parametrical dependence on the compactness

of the grains, on the slope of the bed and on prototypical values of bed roughness length of the model. Second series of experiments focuses on incipient transport for large number of particles composing landforms. Hence, the dependence of criticality on Reynolds number is generalized for incipient transport thresholds for varying landform slopes.

1.1. Analytical model

To determine a theoretical model for the initiation of motion of a single bed–particle due to solid–fluid interaction it is necessary to consider surrounding particles. A sedimentary bed (left Fig. 1) may be considered as a repetition of the pattern shown in right Fig. 1. At an initial stage, only particles at the top are able to move, whereas those grains located on a lower layer restrict partially the motion of the uppermost particles and can not be removed (see lateral constraints in right Fig. 1). Solid particles that are candidates to move have not relative velocity and accelerations respect to the flow of a fluid of density ρ_f. Hence, drag force $\mathbf{f}_d$ and lift force $\mathbf{f}_l$ depend on the flow velocity and its gradient. $\mathbf{f}_d$ and $\mathbf{f}_l$ are applied at the centroid of spheres having a uniform density ρ_{sol}, and are specified below. Geometry of the bed is defined by the radius of the particles R, by the entrainment angle β and by the slope $\tan\alpha$ (Fig. 1). The angle β determines the compacity of the bed and the particle area affected by the flow, and has a range: $0° < \beta < 60°$. Maximum compacity and maximum area exposed to the fluid flow correspond to $\beta = 60°$. For values of β greater than 60° the geometry is incompatible.

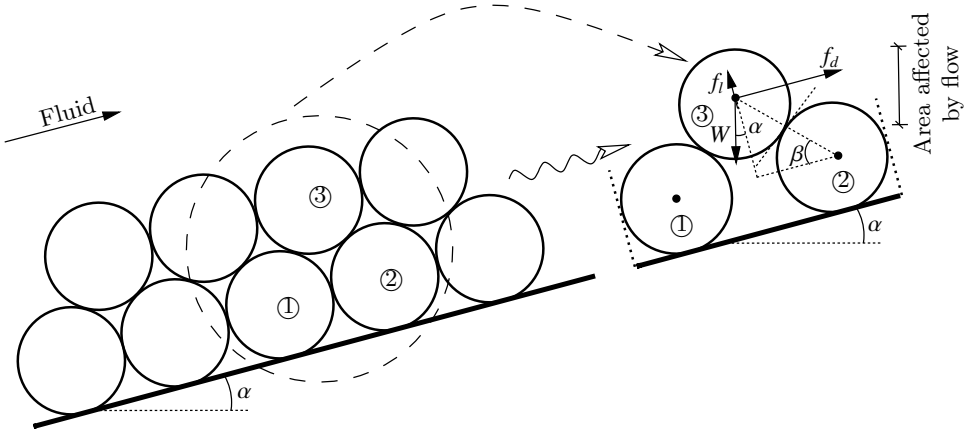

Figure 1: Sediment bed with inclination α (left) composed by the repetition of the simple pattern (right) used in the numerical simulations of Section 3.1.

Balance of forces acting on the particle in the threshold state (see sketch in Fig. 2), considering the plane depicted in Fig. 1 and a Cartesian coordinates system (x, z) such that x positive axis is aligned with the flow direction, is written as

$$\begin{aligned} &\textstyle\sum f_x = 0 \rightarrow |\,\mathbf{f}_d\,| - |\,\mathbf{N}\,|\cos\beta - |\,\mathbf{S}\,|\sin\beta - |\,\mathbf{W}\,|\sin\alpha = 0 \\ &\textstyle\sum f_z = 0 \rightarrow |\,\mathbf{f}_l\,| + |\,\mathbf{N}\,|\sin\beta - |\,\mathbf{S}\,|\cos\beta - |\,\mathbf{W}\,|\cos\alpha = 0 \\ &\textstyle\sum M = 0 \rightarrow (|\,\mathbf{f}_l\,| - |\,\mathbf{W}\,|\cos\alpha)R\cos\beta + (|\,\mathbf{f}_d\,| - |\,\mathbf{W}\,|\sin\alpha)R\sin\beta = 0\ . \end{aligned} \tag{1}$$

In Eqs. (1) $W = \frac{4}{3}\pi R^3(\rho_{sol} - \rho_f)g$ is the submerged weight of the grain, $\mathbf{N}$ is the force normal to the surface of the particle due to contact, $\mathbf{S}$ is the frictional force corresponding to

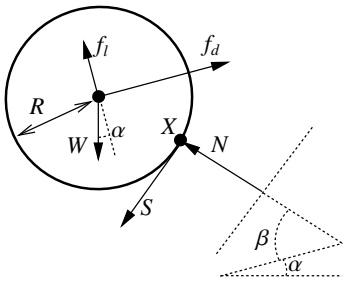

Figure 2: Forces acting on particle, submerged weight W, drag force f_d, lift force f_l normal contact forces N and friction contact force S.

the contact Coulomb's law, tangential to the surface of the particle, $g=\mid \mathbf{g} \mid$ and $\mathbf{g}$ is the acceleration of gravity. $\sum f_x$, $\sum f_z$ and $\sum M$ denote the summation of x components of forces, the summation of z components of forces and the summation of moments about contact point X (Fig. 2) of all applied forces, respectively. Drag and lift forces are given by

$$\mid \mathbf{f}_d \mid = \tfrac{1}{8} C_d \pi d^2 \rho_f V_f^2; \quad \mid \mathbf{f}_l \mid = \alpha_s \rho_f \nu^{0.5} d^2 V_r \left(\frac{\partial u}{\partial z} \right)^{0.5} ,$$

where C_d is a drag coefficient, $d=2R$, V_f is the value of mean velocity around the grain (x direction), α_s is the lift coefficient (Saffman (1968)), ν is the kinematic viscosity of the fluid, and V_r is the value of the difference between mean velocity and velocity at the centroid height (Fig. 3). Momentum transfer ascribed to grain collisions (splash) is not included, given that particles are initially in repose. Starting motion can be by roll or saltation, depending on the total force. In the adopted configuration, the grain can roll or slide over its right neighbor. Otherwise, the grain can detach from the bed if vertical component of resultant force is greater than the submerged weight of the grain, yielding to null $\mathbf{N}$ and absence of contact. To appreciate the effect of entrainment and slope of the landform, consider the balance of moments (third equation of (1)), written as $\mid \mathbf{f}_l \mid \cos\beta + \mid \mathbf{f}_d \mid \sin\beta = \mid \mathbf{W} \mid \cos(\alpha - \beta)$. For $\beta=\alpha=0°$ the grain starts to move if lift force equals weight. For the asymptotic limit given by $\beta=90°$, $\alpha=0°$, the particle would be in an unstable position and rolls without drag. For the limiting case $\beta=60°$, $\alpha=0°$, critical condition is $\mid \mathbf{W} \mid - \mid \mathbf{f}_l \mid > \sqrt{3} \mid \mathbf{f}_d \mid$. For $\alpha \lesseqgtr 0$ necessary $\mathbf{f}_d$ to start the motion decreases/increases, while necessary $\mathbf{f}_l$ decreases in both cases.

1.1.1. Threshold stress

Once basic dynamics has been established, we attain a relation for critical value $\tau_c^\star$ of the wall shear stress $\tau^\star$, as a function of friction Reynolds number for the single particle, $Re^\star = u^\star d/\nu$ (where $u^\star = \sqrt{\tau^\star/\rho_f}$ is the friction velocity), generalizing for variable slope the relationships introduced by Ling (1995). To determine threshold stress, low friction Reynolds number regime and high friction Reynolds number regime must be discriminated to calculate the corresponding drag and lift forces.

For low Reynolds number (about $Re^\star < 3$) laminar flow conditions result in linear velocity distribution around the particle (see upper Fig. 3),

$$\frac{u}{u^\star} = \frac{z u^\star}{\nu},$$

with average velocity and slope

$$V_f = \frac{1}{2}(u_b + u_t) = \frac{u^{\star 2}}{2\nu}(d + 2\delta) \ , \quad \frac{\partial u}{\partial z} = \frac{u^{\star 2}}{\nu} \ ,$$

respectively. Here, u_b and u_t are the velocities at $z{=}\delta$ and $z{=}\delta{+}d$, respectively. The value of δ (Fig. 3) is typically assumed as the equivalent bed roughness length, denoted as z_0. The resulting drag force by considering drag coefficient for laminar regime, $C_d = \dfrac{24\nu}{V_r d}$, and lift force are

$$| \mathbf{f}_d | = \frac{3}{2}\pi\left(1 + 2\frac{\delta}{d}\right)\tau^\star d^2, \quad | \mathbf{f}_l | = \frac{\alpha_s}{2}\frac{u^\star d}{\nu}\left(1 + 2\frac{\delta}{d}\right)\tau^\star d^2 \ , \tag{2}$$

respectively. By replacing drag and lift forces into balance equations (1), the relation $\tau_c^\star$–$Re^\star$ for initiation of motion is acomplished,

$$\frac{\tau_c^\star}{(\rho_{sol} - \rho_f)gd} = \frac{\dfrac{\pi}{6}(\sin\alpha\tan\beta + \cos\alpha)}{\dfrac{3}{2}\pi\left(1 + 2\dfrac{\delta}{d}\right)\tan\beta + \dfrac{\alpha_s}{2}\dfrac{u^\star d}{\nu}\left(1 + 2\dfrac{\delta}{d}\right)} \ . \tag{3}$$

The reader can note that threshold condition depends on slope and on compactness of the array of particles.

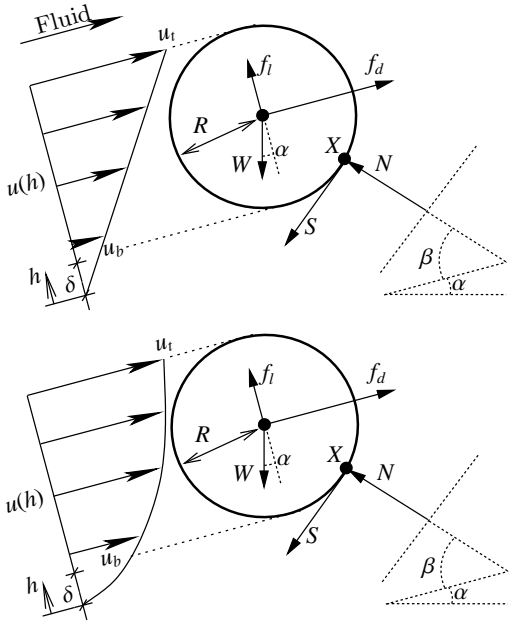

Figure 3: Velocity distribution for low particle Reynolds number (upper) and large particle Reynolds number (lower).

For large particle Reynolds number ($Re^\star \geq 30$) the velocity distribution (lower Fig. 3) is

$$\frac{u}{u^\star} = \frac{1}{\kappa}\log\frac{z}{z_0} \approx 2.5\log\frac{z}{z_0}\ ,$$

where κ=0.41 is the von Karman constant. Mean velocity is computed as

$$V_f = \frac{1}{d}\int_{z=\delta}^{z=d+\delta} u dz = \frac{2.5u^\star\left[(d+\delta)\log(d+\delta) - d(\log(z_0)+1) - \delta\log(\delta)\right]}{d}\ ,$$

and $\partial u/\partial z$ is

$$\frac{\partial u}{\partial z} = \frac{1}{d}\int_{z=\delta}^{z=d+\delta}\frac{\partial u}{\partial z}dz = 2.5\frac{u^\star}{d}\left[\log\left(\frac{d}{z_0}\left(1+\frac{\delta}{d}\right)\right) - \log\frac{\delta}{z_0}\right]\ .$$

Drag and lift forces are

$$|\ \mathbf{f}_d\ | = \frac{1}{2}C_d\pi R^2\rho_f V_f^2 = \frac{1}{8}C_d\pi\frac{{V_f}^2}{{u^\star}^2}\tau^\star d^2;\quad |\ \mathbf{f}_l\ | = \alpha_s\frac{V_f}{u^\star}\left(\frac{\partial u/\partial z}{u^\star}\right)^{0.5}\left(\frac{u^\star d}{\nu}\right)^{-0.5}\tau^\star d^2\ , \tag{4}$$

where $C_d = \dfrac{24\nu}{V_r d}\left[1 + 0.15\left(\dfrac{V_f d}{\nu}\right)^{0.687}\right]$.

By following the same procedure as in laminar case, a nondimensional form of the critical stress as function of $Re^\star$ for turbulent flows is

$$\frac{\tau_c^\star}{(\rho_{sol}-\rho_f)gd} = \frac{\dfrac{\pi}{6}(\sin\alpha\tan\beta + \cos\alpha)}{\dfrac{\pi}{8}C_d\left(\dfrac{V_f}{u^\star}\right)^2\tan\beta + \alpha_s\dfrac{V_f}{u^\star}\left(\dfrac{\partial u/\partial z}{u^\star}\right)^{0.5}\left(\dfrac{u^\star d}{\nu}\right)^{-0.5}}\ , \tag{5}$$

dependent on local slope and compacity.

2. Discrete element method

The present Discrete Element Method simulates the interaction among particles by a soft–sphere model. In spite of a more demanding time integration in compare with hard–sphere model, soft–sphere model is more suitable for long–lasting multiple contacts of particles. Particularly, soft–sphere model is appropiate when many contacts are permanent, as is the case of landforms during incipient motion. Soft–sphere model assumes rigid particles during contact, while deformation is considered by means of force models that simulates contact force through a penalization technique. Penalization enables small overlaps (see left Fig. 4) without the insertion of new unknowns (see Ch. 10 of Belytschko et al. (2000) for discussion and Pérez-Aparicio and Bravo (2006) and references therein for applications in other fields), while long lasting contacts are based on a spring that allows repulsions.

First, we define a gap function $g_N^{ik}(\boldsymbol{X})$ that measures the distance between two bodies i and k, as

$$g_N^{ik}(\boldsymbol{X}) = \left[\boldsymbol{X} - \boldsymbol{Y}(\boldsymbol{X})\right]\boldsymbol{R}^{ik}\ ,$$

where $\boldsymbol{X}$, $\boldsymbol{Y}$ define the coordinates of the set of points belonging to i and k respectively, that are either in contact $g_N^{ik}(\boldsymbol{X}) \approx 0$, or in the closest position to the opposite body

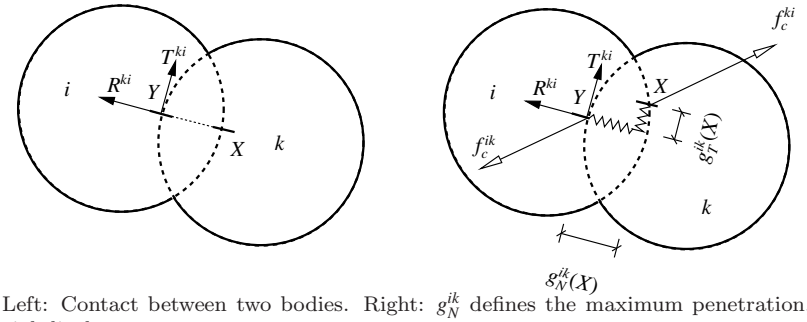

Figure 4: Left: Contact between two bodies. Right: g_N^{ik} defines the maximum penetration, g_T^{ik} defines the tangential displacement.

$g_N^{ik}(\boldsymbol{X}) > 0$, and $\boldsymbol{R}^{ik}=-\boldsymbol{R}^{ki}$ is the normal unit vector at contact point (see Fig. 4). Second, to describe the motion of contact points in the tangential direction it is necessary to add a kinematic condition by introducing the tangential gap $g_T^{ik}(\boldsymbol{X})$ as follows,

$$g_T^{ik}(\boldsymbol{X}) = [\boldsymbol{X} + \boldsymbol{\epsilon}^i(\boldsymbol{X}) - \boldsymbol{Y}(\boldsymbol{X}) - \boldsymbol{\epsilon}^k(\boldsymbol{Y}(\boldsymbol{X}))]\ \boldsymbol{T}^{ik}\ ,$$

where $\boldsymbol{\epsilon}^i(\boldsymbol{X})$ and $\boldsymbol{\epsilon}^k(\boldsymbol{Y}(\boldsymbol{X}))$ are the displacements of the contact points of the bodies i and k respectively and corresponding to a time increment, while $\boldsymbol{T}^{ik}$ is the tangential unit vector at contact point (see left Fig. 4).

Finally, to prescribe non–penetration dynamically, the method imposes contact force defined as

$$\boldsymbol{f}_c^{ik} = f_{cN}^{ik}\ \boldsymbol{R}^{ik} + f_{cT}^{ik}\ \boldsymbol{T}^{ik}\ ,$$

where f_{cN}^{ik} and f_{cT}^{ik} are the components of contact force in normal and tangential direction. In case of two rigid rounded bodies, force is applied at a single point. f_{cT}^{ik} is governed by the frictional Coulomb's law,

$$\Phi^{ik} = f_{cT}^{ik} - \left|f_{cN}^{ik}\right|\mu \le 0\ ; \qquad g_T^{ik} \ge 0\ , \tag{6}$$

where $\left|f_{cN}^{ik}\right|\mu$ is the frictional force, $\mu = \tan\phi$ is the friction coefficient and ϕ is the friction angle. Second condition given by Eqs. (6) enforces motion to be in the direction of tangential contact force component. When $\Phi \ge 0$ sliding starts, while if $\Phi < 0$ rolling occurs.

Constitutive equation for the contact force is simulated by the penalization technique. The key idea is to introduce two parameters, denoted as K_N and K_T, representing two high stiffness elastic springs placed between the contact points of the bodies along normal and along tangential directions respectively (see right Fig. 4). Hence, contact forces are: $\boldsymbol{f}_{cN}^{ik} = K_N g_N^{ik}$ and $\boldsymbol{f}_{cT}^{ik} = K_T g_T^{ik}$ (rolling), or $\boldsymbol{f}_{cN}^{ik} = K_N g_N^{ik}$ and $\boldsymbol{f}_{cT}^{ik} = \mu \boldsymbol{f}_{cN}^{ik}$ (sliding). Calculation of precise contacts is sensitive to a proper tuning of the aforementioned parameters. Governing equations are formulated by Hamiltonian mechanics and are solved by the discrete element method. The formulation results in equations of motion for each body of a set of n_{bd} interacting bodies via the Hamiltonian function H defining

the total energy of the system,

$$H(\boldsymbol{Q}^i(x,y,t),\boldsymbol{P}^i(x,y,t)) = \sum_{i=1}^{n_{bd}} \left[K(\boldsymbol{P}^i(x,y,t)) + V(\boldsymbol{Q}^i(x,y,t)) \right] ,$$

$$K(\boldsymbol{P}^i(x,y,t)) = \frac{1}{2} \int_{\Omega^i} \frac{\boldsymbol{P}^i(x,y,t)^2}{\rho_{sol}} \, \mathrm{d}\Omega ,$$

where $\boldsymbol{Q}^i(x,y,t)$ is the position of the particle i, $\boldsymbol{P}^i(x,y,t)$ is the linear momentum of the particle i, $K(\boldsymbol{P}^i(x,y,t))$ is the kinetic energy, $V(\boldsymbol{Q}^i(x,y,t))$ is the potential energy and Ω^i is the volume Ω of the particle i. The solution $(\boldsymbol{Q}^i(x,y,t),\ \boldsymbol{P}^i(x,y,t))$ corresponds to the minimum energy of the system and is given by the Hamiltonian canonical equations,

$$\dot{\boldsymbol{Q}}^i = \frac{\partial H}{\partial \boldsymbol{P}^i} = \frac{\boldsymbol{P}^i}{\rho_{sol}}; \quad \dot{\boldsymbol{P}}^i = -\frac{\partial H}{\partial \boldsymbol{Q}^i} = -\nabla V(\boldsymbol{Q}^i) \ . \tag{7}$$

We approximate Eqs. (7) by a discrete representation of displacements and linear momentum with nodal shape functions $\boldsymbol{N}^i(x,y)$ such that for each body i,

$$\boldsymbol{Q}^i = \boldsymbol{N}^i \boldsymbol{q}^i; \ \boldsymbol{P}^i = \boldsymbol{N}^i \boldsymbol{p}^i \ . \tag{8}$$

Here $\boldsymbol{q}^i$ and $\boldsymbol{p}^i$ are values of displacements and momentum at the centroid of the particle. Nodal shape function is defined as

$$\boldsymbol{N}^i(x,y) = \begin{bmatrix} 1 & 0 & -(y-y_G) \\ 0 & 1 & (x-x_G) \end{bmatrix}$$

where (x_G, y_G) are the coordinates of the center of gravity. By replacing discretization given by Eqs. (8) in Eqs. (7), we accomplish a discrete system of equations. In matrix form the system is

$$\dot{\boldsymbol{q}} = \boldsymbol{M}^{-1}\boldsymbol{p} \ ; \qquad \dot{\boldsymbol{p}} = \boldsymbol{f}_c + \boldsymbol{f}_d + \boldsymbol{f}_l + \boldsymbol{W} \ , \tag{9}$$

where $\boldsymbol{M}$ is the assembled lumped mass matrix. Time integration of Eqs. (9) is performed by an implicit one step algorithm proposed in Bravo et al. (2011) and Bravo et al. (2012) . To compute the stress field produced by an uniform velocity field perturbed by a landform of a complex shape, it is necessary to use of a numerical methodology. The velocity field is computed by a finite element model for nonbuoyant and nonrotating boundary layer flows, and friction velocity is computed from the log law,

$$u^\star = (u_x^\star, u_y^\star) = \kappa \frac{(\mathbf{u} - \mathbf{u}\cdot\mathbf{n})\big|_{z_e}}{\log(z_e/z_0)} \ . \tag{10}$$

Here the flow velocity $\mathbf{u}$ is evaluated at the node adjacent to the land surface, placed at a distance z_e along the normal direction $\mathbf{n}$ of the land surface. Finally, drag and lift forces are computed by means of, either Eqs. (2) for laminar range, or Eqs. (4) for turbulent range.

3. Numerical experiments

The first series of simulations is conducted for a single spherical particle of non–cohesive sediment resting in an horizontal bed and in a sloped bed. The beds are composed of fixed particles of the same type and have a wide range of compacity. For horizontal bed, numerical computations are compared with prevailing experimental results. The second experiment exploits the ability of the numerical approach to simulate motion of large number of particles, by defining triangular piles with variable slope to determine threshold conditions of incipient transport. For all the simulations, we assume that particle motion is developed in the flow plane.

3.1. Incipient motion

First experiment considers the configuration depicted in Fig. 1 (right) for $\alpha \in [0°,30°]$. Lateral rigid (periodic) boundaries and a high friction coefficient prevent the motion of bottom spheres. An undisturbed boundary layer flow is assumed, given particles on the bottom do not modify substantially the velocity field. Therefore, forces are computed straightforwardly by Eqs. (2) (laminar regime) or Eqs. (4) (turbulent regime). Range of entrainment angle is $\beta \in [45°,60°]$, $d \in [5\times10^{-5}\text{m},10^{-3}\text{m}]$, ρ_{sol}=2500 kg/m^3, ρ_f=1 kg/m^3 (air), ν=10^{-5}m^2/s, ϕ=35° and g=9.81 m/s^2. Time increment for integration of Eqs. (9) is Δt=0.0025 s, and K_N=K_T=10^6 N/m. A minimum diameter of d=5×10^{-5}m is adopted to avoid ill–conditioned discrete system of equations of the DEM. We consider typical range of bed roughness length, $z_0 \in [d/30,d/10]$ (e.g. van Rijn (1984)) and results are reproduced for both limiting values. To simulate very small $Re^\star$ conditions, fluid viscosity is augmented (ν=10^{-3}m^2/s).

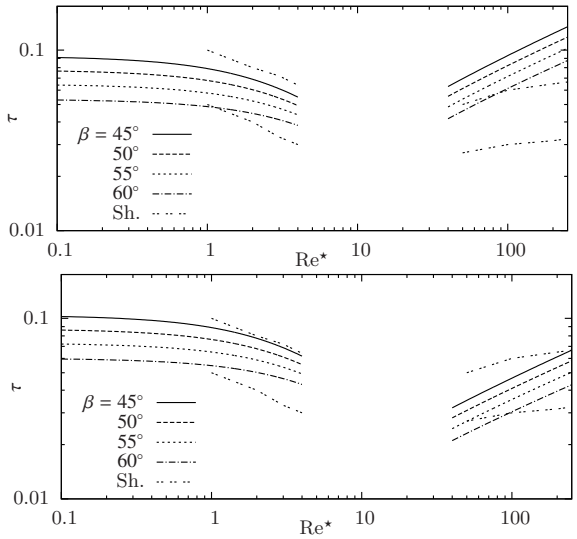

Figure 5: τ–Re* relation by Shields (Sh.) (after Miller et al. (1977)) and analytical from Eqs. (3) and (5) for an horizontal bed α = 0°, $\beta \in [45°,60°]$, z_0=d/10 (top) and z_0=d/30 (bottom).

Figure 5 represents analytical results for nondimensional threshold stress $\tau = \tau_c^\star/(\rho_{sol}-\rho_f)gd$ in terms of $Re^\star$ (top figure is for z_0=d/10 and bottom figure is for z_0=d/30), for different compacities and α = 0°. Figure 6 displays the corresponding numerical computations by DEM. In both figures results are superimposed with the range of experimental

data from Shields (see Miller et al. (1977)). In Fig. 5 and Fig. 6 two regions can be clearly

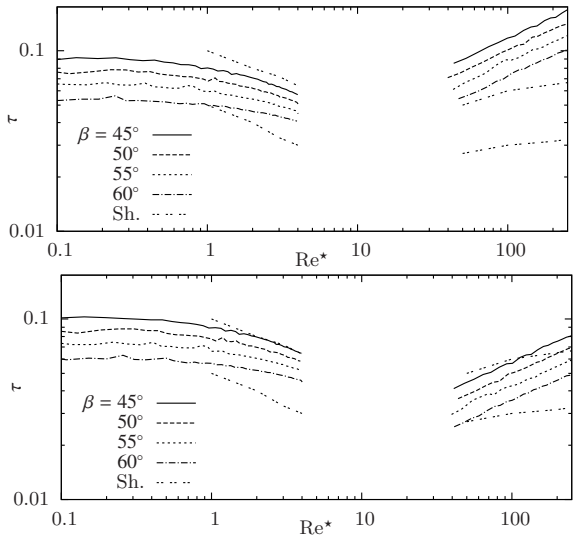

Figure 6: τ–Re* relation by Shields (Sh.) (after Miller et al. (1977)) and numerical (DEM) for an horizontal bed $\alpha = 0°$, $\beta \in [45°,60°]$, z_0=d/10 (top) and z_0=d/30 (bottom).

identified, the low particle Reynolds number region and the high particle Reynolds number region. Between both regions, a range defined approximately as $5<Re^\star<30$ specifies a transition region, where the representation of drag and lift given, either by Eqs. (2) or by Eqs. (4), is not adequate due to a poor assesment of drag and lift coefficients. For very low Reynolds numbers ($Re^\star<3$), τ is nearly constant due to a negligible lift contribution (second term of the denominator of Eq. (3)). Numerical and analytical computations employ drag coefficients for spherical particles, thereby overpredicting to some extent critical stress for large particle Reynolds numbers ($Re^\star>30$) in compare with experimental results by Shields for non fully spherical grains.

Threshold stress depends significantly on compacity, increasing with decreasing β due to a raising opposition of the weight to start the motion of the grains. Furthermore, selection of bed roughness value in its standard range is relevant in the analytical solution and in the numerical solution. The value of critical stress increases if roughness increases, compatible with the growth of boundary layer thickness. Best fit with laboratory results is that of $\beta \in [50°,55°]$ and $z_0 \approx$d/30 for small shear Reynolds number and for large shear Reynolds number. Critical stresses calculated by numerical method are regularly higher than values calculated by analytical method. Departure of numerics from analytical answers is mainly attributed to the technique employed to detect incipient motion. While analytically the threshold can be precisely identified, the numerical procedure (resembling a laboratory technique) distinguishes the initiation of motion by measuring a finite displacement of the particle. This displacement frequently arises after a sequence of rolling and rolling/sliding and before the starting of saltation mode. Value adopted as marker displacement in the numerical approach is of $0.3d$.

Analytical and numerical answers accounting for bed slope are summarized in Figs. 7 and 8 respectively, where nondimensional critical stress in terms of $Re^\star$ is represented for $\alpha \in [15°,30°]$ and β=60° (top figures are for z_0=d/10 and bottom figures are for z_0=d/30).

The numerical detection of threshold yields again to higher values of threshold stress than analytical. Increase of critical values with slope is noteworthy, in agreement with the increase of drag force needed to initiate the motion once α get larger, for a constant entrainment angle β and negligible lift (see Eqs. (1)).

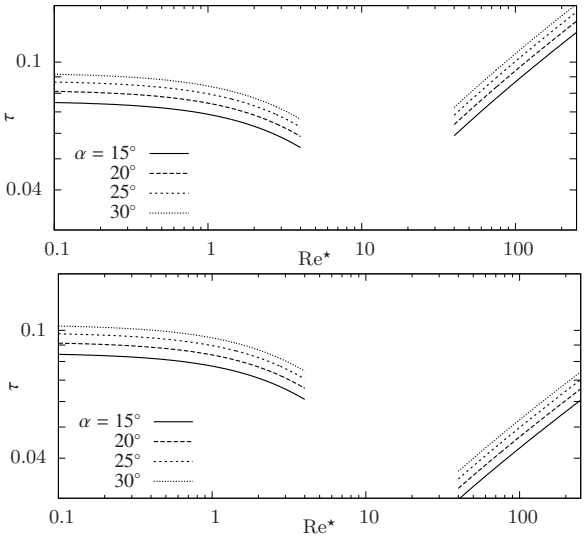

Figure 7: Analytical τ–Re* relation from Eqs. (3) and (5), $\alpha \in [15°,30°]$, β=60°, z_0=d/10 (top) and z_0=d/30 (bottom).

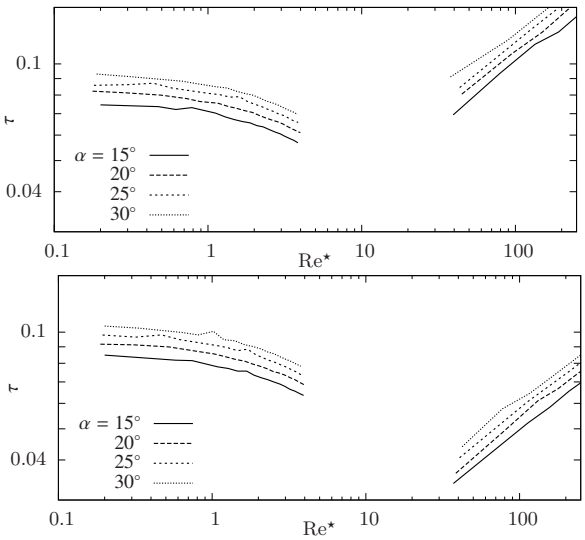

Figure 8: Numerical τ–Re* relation for $\alpha \in [15°,30°]$, β=60°, z_0=d/10 (top) and z_0=d/30 (bottom).

3.2. Incipient transport for landforms

To define the geometry of the problem, particles of diameter d were formed into a triangular pile (see Figs. 9 and 10), parameterized by $d \in [1\times10^{-4}\text{m},10^{-3}\text{m}]$, $\alpha \in [15°,30°]$,

β=60°, $\phi \geq \alpha$ to avoid avalanches, and length of the pile b=$2h/\tan\alpha$, where h is the height of the pile of value 0.02 m. The remaining parameters are the same as foregoing test. Because of the large number of particles involved, minimum diameter is restricted to d=1×10^{-4}m to elude ill-conditioning discrete systems.

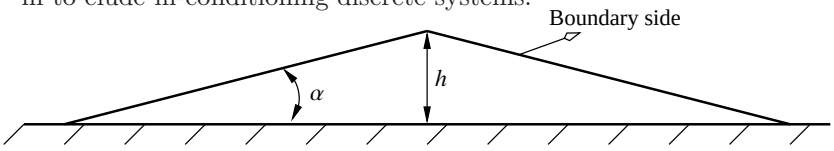

Figure 9: Geometry of the triangular landform defined by height h and slope $\tan\alpha$.

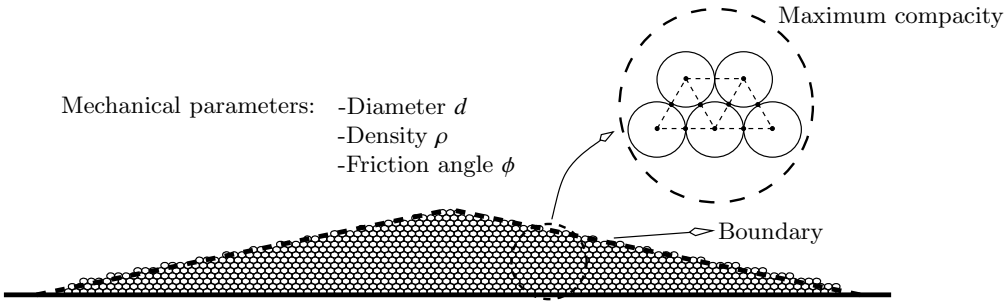

Figure 10: Internal geometry and mechanical parameters that define the behavior of the landform (maximum compacity corresponds to β=60°).

A realistic method to determine a threshold stress for the initiation of motion should be based on the measurement of a distinguishable sediment flux, despite the fact of the indeterminacy to discern (experimentally) the number of moving particles. Prescribed minimum fluxes were considered in the literature (see discussion in Dey (1999)) as, for instance, the value of 0.41×10^{-3} kg s/m, conforming to observations. To generalize the determination of the critical condition, we propose to establish the relation for the nondimensional threshold stress as a function of a percentage of moving particles and of $Re^\star$, ranging from a single particle to all the set of particles. Because the initial motion is produced by rolling and sliding mechanisms of particles situated on the windward slope of the bedform, the rate of moving grains is computed among grains initially belonging to this surface. However, the presence of the landform as an obstacle to the fluid flow yields a variable shear stress over the bed surface. Ergo a more detailed computation of stress and a criterion to specify an average critical stress are required.

First requirement is attained by the numerical computation of the flow along the surface with a finite element model based on the characteristic split method (CBS), (see e g. Ortiz et al. (2006), Zienkiewicz et al. (1999)) for incompressible flows over two spatial dimensions. To look after potential intricacies of the geometry, we adopt unstructured triangular meshes. Figure 11 shows the mesh for the experiment, where details in the vicinity of the pile are represented on the right. The depicted mesh comprises 4566 nodes and 8863 triangular elements of average element size length[1] $\overline{\delta}$ value of 0.004 m. Nodes

[1] Average element side length is defined as $\overline{\delta} = \frac{1}{E}\sum_{j=1}^{E}\sqrt{(\Delta x)_j^2+(\Delta y)_j^2}$, where E is the total number of elements, and $\Delta x, \Delta y$ are the maximum distance between vertices of the triangle along x and y respectively.

belonging to elements with at least one vertex on the boundary surface are picked out to compute stress by the log law given by Eq. (10). For these points, we calculate z_e as well as the corresponding velocity component in the tangential direction of the closer element side belonging to the boundary: $(\mathbf{u} - \mathbf{u}\cdot\mathbf{n})\big|_{z_e}$. In the fluid model, definition of boundary conditions are as follows (see Fig. 12).

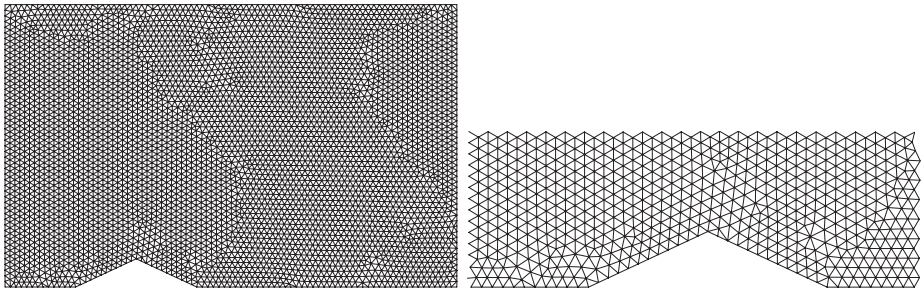

Figure 11: Unstructured finite element mesh (left) and mesh details surrounding landform (right).

For the upper boundary impermeable free-slip lid is imposed whereas lateral boundaries are periodic in the streamwise and spanwise direction, assuming a fully developed flow with an ambient velocity field U_e fixed for a given shear Reynolds number. Remaining portion of the boundary corresponds to the bottom and has no–slip condition. Calculation of stresses over these surfaces is performed once steady state flow is reached by the time–iterative CBS procedure. Critical stress is defined by the average value for n particles displaced at least $0.3d$, and consequently, in terms of the percentage of moving particles, $n/N(d)$, where $N(d)$ is the total amount of particles of a given diameter d constituting the exposed surface.

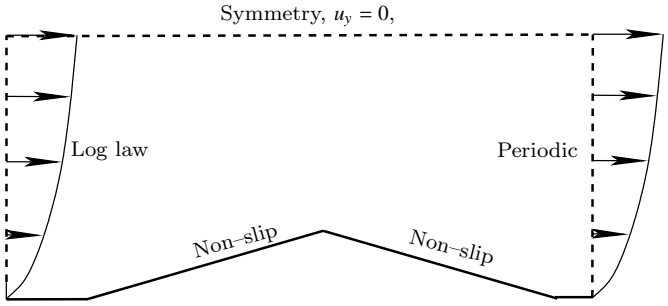

Figure 12: Boundary conditions.

Figure 13 depicts motion of the grains for one of the simulations at the instant when initiation of sediment transport is measured. Grains at the top of the pile starts the process, where usual largest velocity gradients and maximum exposition take place. Limiting conditions for single particles propagates downward, reaching finally the prescribed number of moving grains. Particles at or closer to the crest usually lift after a short rolling phase, while for particles at the mid slope significant displacements by rolling prevail. Detailed numerical results are plotted in Fig. 14 that summarize the behavior of the activated fraction of particles for the range of diameters considered and for α=15° (remaining slopes are not shown for brevity), in terms of $Re^\star$ and in terms of τ, respectively (top

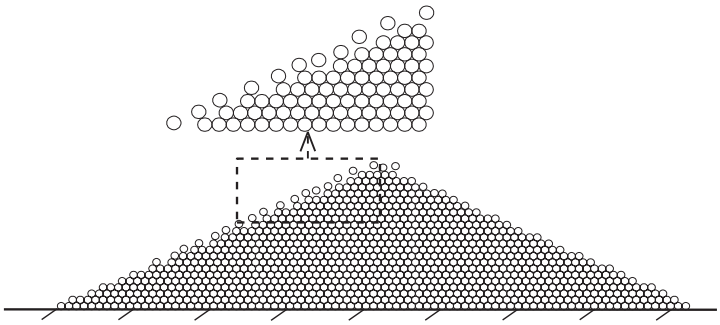

Figure 13: Motion of grains at the instant when initiation of sediment transport is measured.

figures are for z_0=d/10 and bottom figures are for z_0=d/30). Figure 15 (for z_0=d/10) and Figure 16 (for z_0=d/30) represent the nondimensional average threshold stress in terms of particle Reynolds number for α=15°, 20° and 25° respectively and for percentage of moving grains of value 10%, 30%, 50% and 70%.

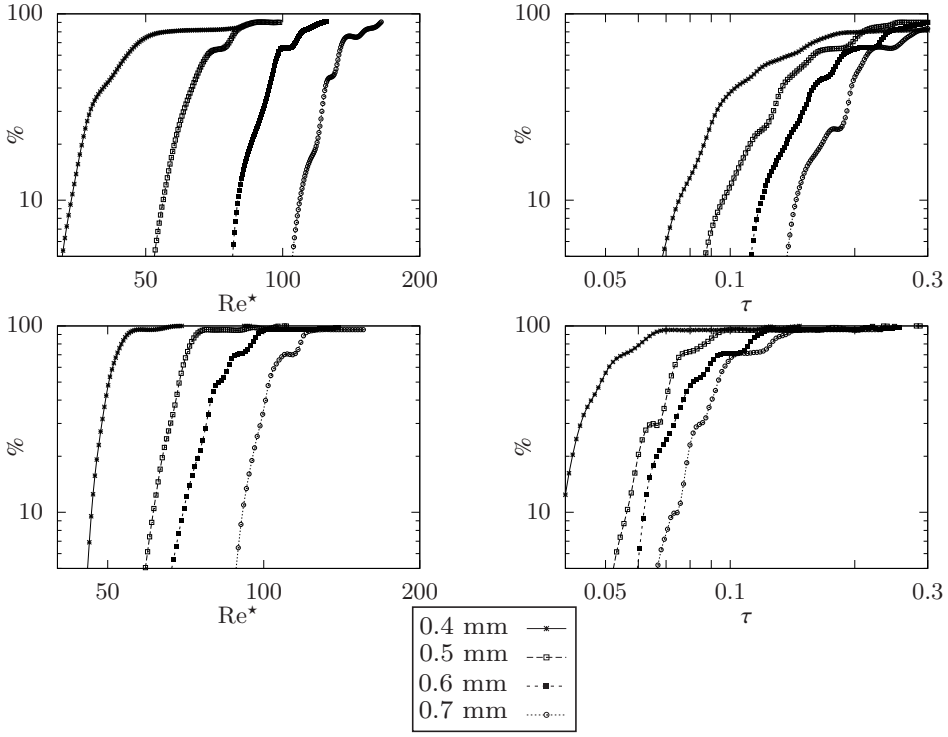

Figure 14: Fraction of moving particles in function of $Re^\star$ (left) and τ (right) for a series of particle size, for α=15° and z_0=d/10 (top) and z_0=d/30 (bottom).

Threshold stress increases with the slope because of the subsequent increment of resistance, as was already perceived in the single–particle experiments. Besides, behavior of critical stress for low and high shear Reynolds number regimes is homologous with single particle answer, but shows higher limiting values due to the average procedure of computation. For high Reynolds regime, Fig. 14 reveals some wiggles in case of particles

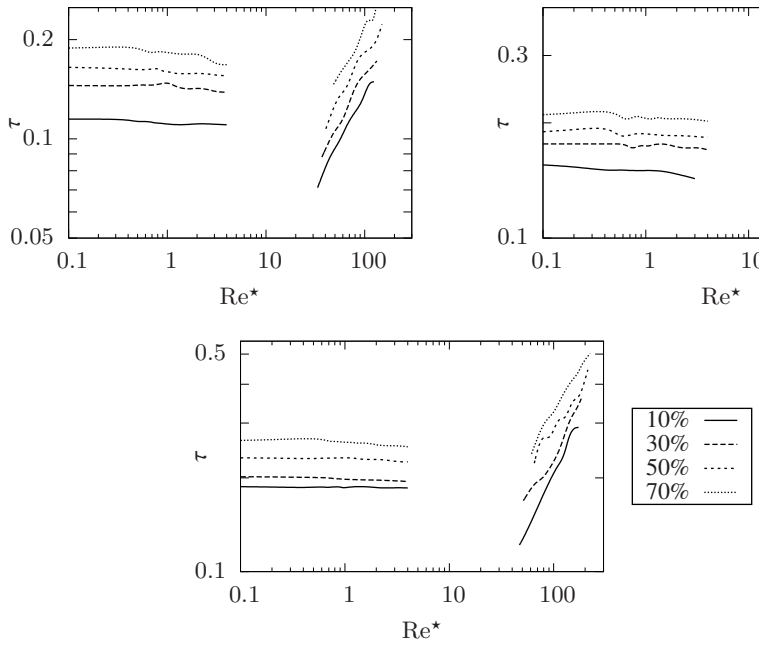

Figure 15: Numerical τ–$Re^\star$ for a series of fraction of moving particles, z_0=$d/10$ and for α=15° (top–left), α=20° (top–right) and α=25° (bottom).

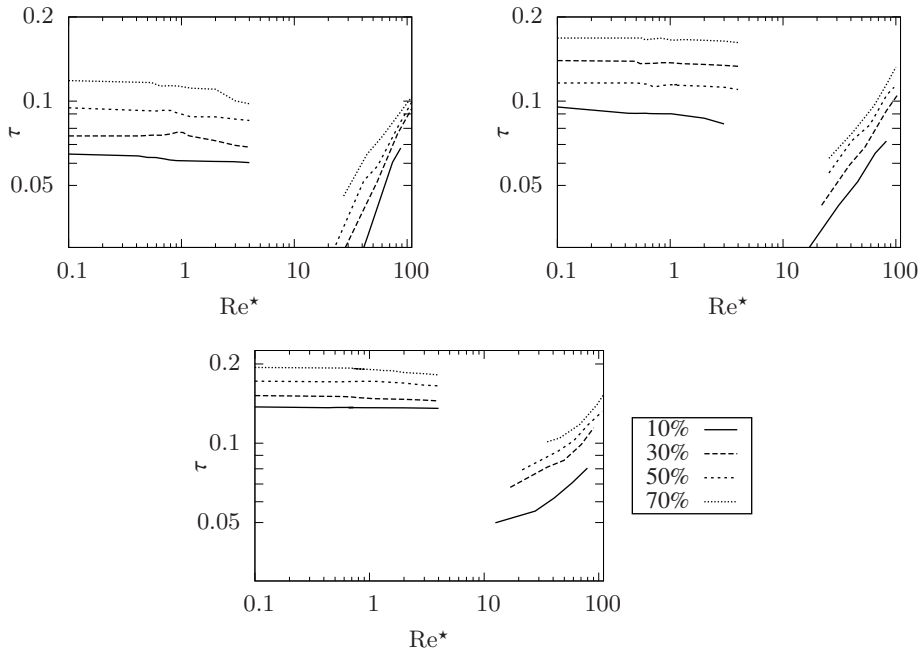

Figure 16: Numerical τ–$Re^\star$ for a series of fraction of moving particles, z_0=$d/30$ and for α=15° (top–left), α=20° (top–right) and α=25° (bottom).

with d>0.5 mm. These small oscillations are ascribed to the counting method; for big diameters a small number of grains is sufficient to construct the ripple, but percentage of moving grains can not be precisely determined. A smooth saturation effect (Fig. 14) is noticeable for the highest range of stress, and especially for larger particles. Thus, these particles (placed in the windward foot of the pile) do not move because the boundary layer is not sufficiently thin. For higher slopes, the saturation effect is reached for lower percentages of mobilized grains, consistent with the modified flow distribution. Further, higher values of bed roughness yield to higher values of stress needed to move the same percentage of particles, as a result of the increase of boundary layer thickness. Consequently, saturation effect is detected for higher values of shear stresses. In practice, the saturation is not significant because it is reached at percentages of moving particles such that initiation of motion is accompanied by movement of particles belonging to lower layers. Thus, distinct shape variations violates the essence of the definition of incipient transport. For the same nondimensional stress, fraction of moving grains decreases with increasing slope (Figs. 15 and 16) in correspondence with growing resistance by gravity aforementioned. Limiting values of stress raise significantly for higher slopes and for the same percentage of mobilized particles.

4. Concluding remarks

Discrete element method has the ability to simulate motion and interaction of a large number of particles. The present work exploits this value, by extending incipient conditions of sediment transport due to fluid flow to small bedforms of general shape. Analytical determination of drag and lift forces for a single particle is a previous requisite for the micro-dynamics model. The key premise is to enable its use to grains with varying compacity resting on local variable bed slope. Analytical and numerical results substantiate these enhancements, showing that threshold stress depends remarkably on compacity and local slope.

To determine threshold stress for bedforms the proposed technique computes percentage of moving particles belonging to the exposed surfaces, introducing an experimental practice to the numerical methodology. As a consequence of the procedure, several parametric results can be chosen. At first, we presented fraction of moving particles with varying diameter in terms of friction Reynolds number or in terms of critical shear stress. However, the most illustrative option is critical stress in terms of friction Reynolds number for varying fraction of moving particles and slope, because it represents a novel extended Shields diagram. Although counting of particles for the numerical approach follows the experimental process, percentage of moving grains and corresponding threshold stress can be precisely established, except for some few pathological cases, such as very small piles conformed by grains with very large diameters.

Furthermore, a wide variety of initial configurations can be adopted to mimic natural beds or the existence of obstacles to the flow. These configurations can be simply defined as initial conditions for flow model and sediment model. The straighforward methodology is justified by two main reasons. First, because of the particularly convenient properties of the method for problems with intrinsic discontinuous geometry. Second, because we are evaluating inception of motion (via incipient motion or via instantaneous incipient transport), for which coupling between flow field and evolutionary boundary forcings is not relevant. Consequently, the developments presented in this paper expand readily to

the determination of incipient motion for a broad range of sediment transport problems past bedforms.

Subsequent saltation mode and suspension mode of the mobilized particles further imply more detailed flow description and a stronger coupling of the evolution of the bed with the flow model. Although this task is mature for large scale morphologies by means of continuous procedures (see Ortiz and Smolarkiewicz (2009)), description of a mid–size evolutionary form (typically smaller than minimum size to reach a meta–stable state) including its micro–mechanics by a coupled continuous–discontinuous approach still call for improvement.

5. Acknowledgements

This work was partially supported by the MICIIN Grants #BIA-2008-00522 and #BIA-2012-32918.

References

Belytschko, T., Liu, W., Moran, B., 2000. Nonlinear Finite Elements for Continua and Structures. Wiley.

Bravo, R., Pérez-Aparicio, J., Laursen, T., 2011. An enhanced energy conserving time stepping algorithm for frictionless particle contacts. International Journal for Numerical Methods in Engineering 85 (11), 1415–1435.

Bravo, R., Pérez-Aparicio, J., Laursen, T., 2012. An energy consistent frictional dissipating algorithm for particle contact problems. International Journal for Numerical Methods in Engineering 92 (9), 753–781.

Dey, S., 1999. Sediment threshold. Applied Mathematical Modelling 23 (5), 399–417.

Ikeda, S., 1982. Incipient motion of sand particles on side slopes. Journal of Hydraulic Division ASCE 108 (1), 95–114.

Ling, C. H., 1995. Criteria for incipient motion of spherical sediment particles. Journal of Hydraulic Engineering-ASCE 121 (6), 472–478.

Mantz, P. A., 1977. Incipient transport of fine grains and flakes by fluids – extended shields diagram. Journal of Hydraulic Division ASCE 103 (6), 601–615.

Marsh, N. A., Western, A. W., Grayson, R. B., 2004. Comparison of methods for predicting incipient motion for sand beds. Journal of Hydraulic Engineering-ASCE 130 (7), 616–621.

Miller, M. C., Mccave, I. N., Komar, P. D., 1977. Threshold of sediment motion under unidirectional currents. Sedimentology 24 (4), 507–527.

Moosavi, M., Grayeli, R., 2006. A model for cable bolt–rock mass interaction: Integration with discontinuous deformation analysis (dda) algorithm. International Journal of Rock Mechanics and Mining Sciences 43, 661–670.

Ortiz, P., Smolarkiewicz, P., 2006. Numerical simulation of sand dune evolution in severe winds. International Journal for Numerical Methods in Fluids 50 (10), 1229–1246.

Ortiz, P., Smolarkiewicz, P., 2009. Coupling the dynamics of boundary layers and evolutionary dunes. Physical Review E - Statistical, Nonlinear, and Soft Matter Physics 79 (4).

Ortiz, P., Zienkiewicz, O., Szmelter, J., 2006. Hydrodynamics and transport in estuaries and rivers by the cbs finite element method. International Journal for Numerical Methods in Engineering 66, 1569–1586.

Pérez-Aparicio, J., Bravo, R., 2006. Discrete elements. In: TCN, C. (Ed.), Practical Aplications Using Computational Contact Mechanics. Vol. 2.

Saffman, P., 1968. Corrigendum, the lift on a small sphere in a slow shear flow. Journal of Fluid Mechanics 31, 624.

Shi, G., 1988. Discontinuous deformation analysis–a new model for the statics and dynamics of block systems. Thesis (ph.d.), University of California, Berkeley.

Shi, G., Goodman, R., 1985. Two dimensional discontinuous deformation analysis. International Journal of Analysis Methods in Geomechanics 9, 541–556.

Shields, A., 1936. Application of similarity principles and turbulence research to bed-load movement. Tech. rep., Lab. for Hydraulic Water Resources.

van Rijn, L., 1984. Sediment transport. part i: bed load transport. Journal of Hydraulic Engineering-ASCE 110 (10), 1431–1456.

Wallbridge, S., Voulgaris, G., Tomlinson, B. N., Collins, M. B., 1999. Initial motion and pivoting characteristics of sand particles in uniform and heterogeneous beds: experiments and modelling. Sedimentology 46 (1), 17–32.

Wiberg, P., Smith, J., 1985. A theoretical model for saltating grains in water. Journal of Geophysical Research 90, 7341–7354.

Yalin, M. S., Karahan, E., 1979. Inception of sediment transport. Journal of Hydraulic Division ASCE 105 (11), 1433–1443.

Zienkiewicz, O., Nithiarasu, P., Codina, R., Vázquez, M., Ortiz, P., 1999. The characteristic-based-split procedure: An efficient and accurate algorithm for fluid problems. International Journal for Numerical Methods in Fluids 31 (1), 359–392.